MIDIS: The relation between strong (Hβ + [O iii]) emission, star formation, and burstiness around the epoch of reionization

Caputi, K.I.; Rinaldi, P.; Iani, E.; Pérez-González, P.G.; Östlin, G.; Colina, L.; ... ; Ray, T.P.

MIDIS: The Relation between Strong (Hβ + [O III]) Emission, Star Formation, and Burstiness around the Epoch of Reionization

K. I. Caputi[1,2] , P. Rinaldi[1] , E. Iani[1] , P. G. Pérez-González[3] , G. Östlin[4] , L. Colina[2,3] , T. R. Greve[2,5] ,
H. U. Nørgaard-Nielsen[2,5] , G. S. Wright[6] , J. Álvarez-Márquez[3] , A. Eckart[7] , J. Hjorth[8] , A. Labiano[9] , O. Le Fèvre[10] ,
F. Walter[11] , P. van der Werf[12] , L. Boogaard[11] , L. Costantin[3] , A. Crespo Gómez[3] , S. Gillman[2,5] , I. Jermann[2,5] ,
D. Langeroodi[8] , J. Melinder[4] , F. Peissker[7] , M. Güdel[11,13,14] , Th. Henning[11] , P. O. Lagage[15] , and T. P. Ray[16]
[1] Kapteyn Astronomical Institute, University of Groningen, P.O. Box 800, 9700AV Groningen, The Netherlands; karina@astro.rug.nl
[2] Cosmic Dawn Center (DAWN), Copenhagen, Denmark
[3] Centro de Astrobiología (CAB), CSIC-INTA, Ctra. de Ajalvir km 4, Torrejón de Ardoz, E-28850 Madrid, Spain
[4] Department of Astronomy, Stockholm University, Oscar Klein Centre, AlbaNova University Centre, 106 91 Stockholm, Sweden
[5] DTU-Space, Elektrovej, Building 328 , 2800 Kgs. Lyngby, Denmark
[6] UK Astronomy Technology Centre, Royal Observatory Edinburgh, Blackford Hill, Edinburgh EH9 3HJ, UK
[7] I.Physikalisches Institut der Universität zu Köln, Zülpicher Str. 77, 50937 Köln, Germany
[8] DARK, Niels Bohr Institute, University of Copenhagen, Jagtvej 128, 2200 Copenhagen, Denmark
[9] Telespazio UK for the European Space Agency (ESA), ESAC, Camino Bajo del Castillo s/n, 28692 Villanueva de la Cañada, Spain
[10] Aix Marseille Université, CNRS, LAM (Laboratoire d'Astrophysique de Marseille) UMR 7326, 13388 Marseille, France
[11] Max-Planck-Institut für Astronomie, Königstuhl 17, 69117 Heidelberg, Germany
[12] Leiden Observatory, Leiden University, PO Box 9513, 2300 RA Leiden, The Netherlands
[13] Department of Astrophysics, University of Vienna, Türkenschanzstr. 17, A-1180 Vienna, Austria
[14] ETH Zürich, Institute for Particle Physics and Astrophysics, Wolfgang-Pauli-Str. 27, 8093 Zürich, Switzerland
[15] AIM, CEA, CNRS, Université Paris-Saclay, Université Paris Diderot, Sorbonne Paris Cité, F-91191 Gif-sur-Yvette, France
[16] Dublin Institute for Advanced Studies, 31 Fitzwilliam Place, D02 XF86 Dublin, Ireland

Abstract

We investigate the properties of strong (Hβ + [O III]) emitters before and after the end of the "Epoch of Reionization" from $z = 8$ to $z = 5.5$. We make use of ultradeep JWST/NIRCam imaging in the parallel field (P2) of the MIRI Deep Imaging Survey (MIDIS) in the Hubble eXtreme Deep Field (H-XDF), in order to select prominent (Hβ + [O III]) emitters (with rest-frame equivalent width (EW$_0$) $\gtrsim 100$ Å) at $z = 5.5$–7, based on their flux density enhancement in the F356W band with respect to the spectral energy distribution continuum. We complement our selection with other (Hβ + [O III]) emitters from the literature at similar and higher ($z = 7-8$) redshifts. We find (nonindependent) anticorrelations between EW$_0$(Hβ + [O III]) and both galaxy stellar mass and age, in agreement with previous studies, and a positive correlation with specific star formation rate (sSFR). On the SFR–$M^\star$ plane, the (Hβ + [O III]) emitters populate both the star formation main sequence and the starburst region, which become indistinguishable at low stellar masses ($\log_{10}(M^\star) < 7.5$). We find tentative evidence for a nonmonotonic relation between EW$_0$(Hβ + [O III]) and SFR, such that both parameters correlate with each other at SFR $\gtrsim 1$ $M_\odot$ yr^{-1}, while the correlation flattens out at lower SFRs. This suggests that low metallicities producing high EW$_0$(Hβ + [O III]) could be important at low SFR values. Interestingly, the properties of the strong emitters and other galaxies (33% and 67% of our $z = 5.5$–7 sample, respectively) are similar, including, in many cases, high sSFR. Therefore, it is crucial to consider both emitters and nonemitters to obtain a complete picture of the cosmic star formation activity around the Epoch of Reionization.

1. Introduction

Investigating the properties of galaxies in the early Universe is necessary to understand the first steps of galaxy evolution and their link to the process of reionization. Until very recently, these studies were limited to the brightest galaxies at rest-frame UV wavelengths, given the lack of sensitive telescopes operating at $\lambda \gtrsim 2$ μm. The new JWST observations are now radically transforming this field by giving us access to much fainter sources, including the precursor seed units that have eventually grown into more massive galaxies at later cosmic times.

Two of the most fundamental galaxy properties that define galaxy growth are the already assembled stellar mass ($M^\star$) and the ongoing star formation rate (SFR). Although these two properties are known to be related (e.g., Brinchmann et al. 2004; Speagle et al. 2014; Renzini & Peng 2015), it is unclear whether the corresponding physical conditions for star formation are the same at all scales, particularly at high redshifts. Investigating the relation between different galaxy physical parameters and these more fundamental properties is crucial to explain how galaxy evolution took place at early cosmic times.

The search for line emitters provides a shortcut for selecting star-forming galaxies. Especially the presence of the brightest emission lines, such as the Balmer lines, as well as [O II] $\lambda3727$ and [O III] $\lambda\lambda4959$, 5007, helps boosting the galaxy detectability. However, the detection of such emission lines appearing in the rest-frame optical regime has traditionally

been difficult beyond intermediate redshifts, also because of the wavelength coverage and sensitivity of existing telescopes. Now JWST has turned the study of rest-frame optical emission lines to be routinely possible in galaxies up to very high redshifts.

Many studies conducted over the past decade concluded that some emission lines become increasingly important with redshift, i.e., they are more luminous and have higher equivalent widths (EWs; e.g., Roberts-Borsani et al. 2016; De Barros et al. 2019; Matthee et al. 2023). This is particularly the case of the (Hβ + [O III]) line complex (e.g., Smit et al. 2014; Khostovan et al. 2016; Reddy et al. 2018; Endsley et al. 2021). Most of these studies have been based on photometric data, as a less costly alternative to spectroscopy. The presence of prominent emission lines (i.e., emission lines with high EW) can be inferred from photometric measurements via the flux density excess with respect to the spectral continuum, which is produced in the photometric band in which the line is observed (e.g., Sobral et al. 2013; Smit et al. 2014, 2016; Caputi et al. 2017).

The success of this technique has now triggered a number of studies of high-redshift line emitters based on JWST images, reaching galaxies up to the "Epoch of Reionization" ($z \sim 7$). These works have analyzed the dependence of the line emission on general galaxy properties, such as rest-frame UV absolute magnitudes and stellar mass, and inferred the ionizing photon production efficiency to constrain the role of the emitters in the process of reionization (e.g., Prieto-Lyon et al. 2023; Endsley et al. 2023a; Rinaldi et al. 2023). Yet, it has been recently pointed out that line emitters may provide a biased view of the star formation activity at high redshifts (Sun et al. 2023). Putting them in the context of all galaxies present at the same redshifts could, thus, be necessary to understand their importance and achieve a complete picture of early galaxy evolution.

Another aspect that has become evident in the past years is the increasing importance of starburst galaxies with redshift (e.g., Caputi et al. 2017; Rinaldi et al. 2022). These are galaxies whose star formation activity is temporarily enhanced, such that they are placed significantly above the so-called main sequence (MS) of star formation (e.g., Peng et al. 2010; Speagle et al. 2014; Salmon et al. 2015; Rinaldi et al. 2022). Although in the literature there are different definitions for starburst galaxies, a clear way to select them is via their specific star formation rate (sSFR), which has been empirically defined to be $\log_{10}(\text{sSFR}(\text{yr}^{-1})) > -7.6$ (Caputi et al. 2017, 2021). This implies a stellar-mass doubling time (i.e., the inverse of the sSFR) of $\lesssim 4 \times 10^7$ yr, which is roughly compliant with the timescales for starburst episodes studied in the local Universe (e.g., Heckman et al. 1998; Kennicutt 1998; Leitherer et al. 2002; Östlin et al. 2003). The incidence of starbursts is higher among low-stellar-mass galaxies (Bisigello et al. 2018) and the recent JWST studies provide hints that the starburst mode of star formation could be very important in the early Universe (e.g., Endsley et al. 2023b; Dressler et al. 2024).

The goal of this paper is to investigate the connection between prominent (Hβ + [O III]) emission and other properties, including the SFR and sSFR, in galaxies before and after the end of the Epoch of Reionization from $z = 8$ to $z = 5.5$. For this purpose we analyze the deepest existing JWST imaging data, which allow us to select galaxies down to unprecedented low-stellar-mass limits at those redshifts. Moreover, we
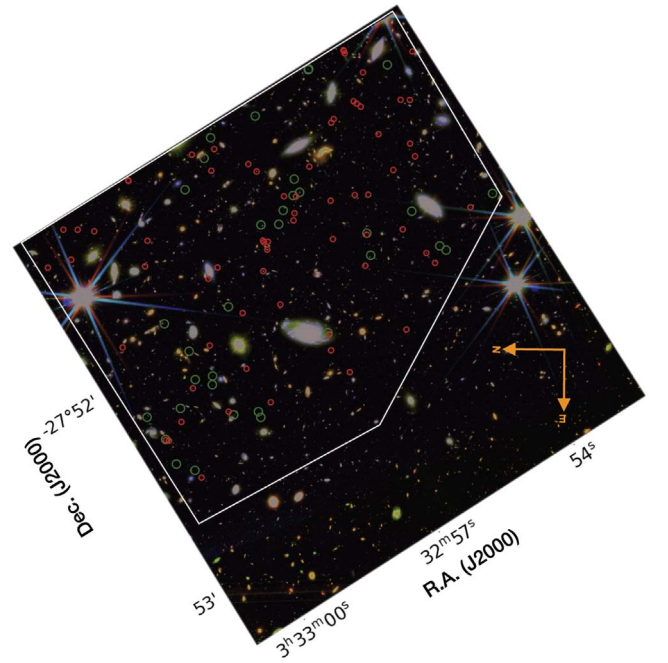

Figure 1. Red, green, and blue composite image of the P2 field with NIRCam coverage. The region delimited with a white line has the deepest coverage in the NIRCam bands and is the field considered in this work. Green circles indicate the location of our (Hβ + [O III]) emitters at $z = 5.5-7.0$, while the red circles correspond to all other sources in the same redshift range.

compare the properties of these emitters to those of all other galaxies at the same redshifts, in order to understand their role in the early steps of galaxy evolution. Throughout this paper we adopt a cosmology with $H_0 = 70$ km s^{-1} Mpc^{-1}, $\Omega_M = 0.3$, and $\Omega_\Lambda = 0.7$. All magnitudes in this paper are total and are expressed in the AB system (Oke & Gunn 1983). Stellar masses and SFRs refer to a Chabrier (2003) initial mass function (IMF).

2. Data Sets

We made use of the ultradeep JWST/NIRCam images that have been taken in parallel with the JWST Guaranteed Time Observations (GTO) program MIRI Deep Imaging Survey (MIDIS; PID: 1283, PI: Göran Östlin) in the Hubble eXtreme Deep Field (H-XDF). We also analyzed data from the Next Generation Deep Extragalactic Exploratory Public (NGDEEP; PID: 2079; PIs: S. Finkelstein, C. Papovich, and N. Pirzkal) survey. All these NIRCam images partly or entirely cover the second Hubble Ultra Deep Field (HUDF) parallel field (hereafter P2; Whitaker et al. 2019). Observations have been taken in a total of six JWST/NIRCam broad bands: F115W, F150W, F277M, and F356M (MIDIS), and F200W and F444W (NGDEEP). More information about these data can be found in Pérez-González et al. (2023) and Austin et al. (2023). Here we restrict our analysis to the $\simeq 3.3$ arcmin^2 area that has maximum homogeneously deep coverage in the NIRCam filters (P2/NIRCam hereafter; Figure 1).

The JWST data presented in this work were obtained from the Mikulski Archive for Space Telescopes at the Space Telescope Science Institute. The MIDIS data set can be obtained via doi:10.17909/je9x-d314 while the NGDEEP data can be accessed via doi:10.17909/v7ke-ze45.

We have processed all these NIRCam images with a modified version of the official JWST pipeline[17] based on jwst 1.8.2 (Bushouse et al. 2022) and Calibration Reference Data System pipeline mapping 1084. Detailed information about the reference files is available at STScI/CRDS. Compared to the official JWST pipeline, our version includes a number of extra steps to deal with some of the problems that still affected the official software. We minimized the impact of the so-called "snowballs" and "wisps,"[18] as well as the $1/f$ noise and residual cosmic rays. After reducing all the NIRCam images, we drizzled and mosaiced all the resulting calibrated files to $0.\!''03$ pixel^{-1}, which is the final pixel scale of our images for science analysis. All these final images have been aligned to the Hubble Legacy Fields (HLF) catalog (Illingworth 2015).[19]

We tested our data reduction by comparing the photometry for the brightest sources (<24 mag) in all the NIRCam filters, following the same approach that we already adopted in Rinaldi et al. (2023). To do that, we produced two versions of the NIRCam images, with and without the aforementioned extra steps. Finally, we extracted the sources by using the software Source Extractor (SExtractor; Bertin & Arnouts 1996) and compared their photometry. This test confirmed that our extra steps do not introduce any systematic effect in the photometry.

As a complement, we also considered Hubble Space Telescope (HST) images over the HUDF/P2 from the HLF GOODS-S (HLF-GOODS-S).[20] The HLF-GOODS-S data in HUDF/P2 are comprised of images in 10 HST broad bands covering the optical (Advanced Camera for Surveys (ACS)/Wide Field Channel (WFC) F435W, F606W, F775W, F814W, and F850LP), and near-infrared (WFC3/IR F098M, F105W, F125W, F140W, and F160W). See Whitaker et al. (2019) for more detailed information on these observations. In this work we only make use of the ACS/WFC images because of two reasons: the WFC3/IR coverage in HUDF/P2 is not as homogeneous as for the ACS/WFC filters and the WFC3/IR images are significantly shallower than the JWST/NIRCam images. In summary, our finally considered image set has coverage in the wavelength range 0.4 μm through 4.4 μm, with a total of 11 broad bands (five HST + six JWST filters).

Our JWST NIRCam imaging in HUDF/P2 is to our knowledge the deepest NIRCam data currently available: their depth is 30.2 and 30.8 mag (5σ), in F150W and F2777W, respectively (Pérez-González et al. 2023). This is about 2 mag deeper than the NIRCam images utilized in Endsley et al. (2023a) and about 1 mag deeper than the JEMS images (Williams et al. 2023).

3. Photometry and Spectral Energy Distribution Fitting

We performed the source detection and photometric measurements using the software SExtractor (Bertin & Arnouts 1996), which we used in dual mode on all bands. In all cases, for the source detection we adopted a superstack image that we created by combining all NIRCam bands. To construct our photometric catalog we used a combination of aperture

photometry in $0.\!''5$ diameter circular apertures and Kron apertures (i.e., MAG_AUTO; Kron 1980), following a similar prescription to that adopted by Rinaldi et al. (2022, 2023). For sources with mag < 27, we chose the brightest among the circular-aperture flux (+aperture correction) and the Kron flux. For fainter sources, we always adopted the circular-aperture flux (+aperture correction). We determined the limiting magnitude above which only aperture fluxes are considered based on tests performed on the HST photometry (see Rinaldi et al. 2023 for details). Finally, all our fluxes have been corrected for Galactic extinction.

We adopted a minimum error of 0.05 mag for all the HST photometry because SExtractor typically underestimates the photometric errors (e.g., Sonnett et al. 2013). We decided to adopt this minimum error for the NIRCam images as well to account for possible uncertainties in the flux calibration. For nondetected sources in any given band, we estimated flux upper limits by performing empty-aperture statistics. We placed multiple ($0.\!''5$ diameter) random circular apertures on the corresponding background image to estimate the background rms (1σ), which in our case is about 32.0–32.5 mag, depending on the NIRCam band.

We performed the spectral energy distribution (SED) fitting of our sources using the code LePHARE (Arnouts & Ilbert 2011), following a similar prescription to that described in Rinaldi et al. (2022, 2023). We considered the synthetic model templates by Bruzual & Charlot (2003, hereafter BC03), making use of two different star formation histories (SFHs): a standard exponentially declining SFH (with eight different τ values) and a single stellar population. We adopted two distinct metallicity values, solar metallicity ($Z_\odot = 0.02$) and a fifth of solar metallicity ($Z = 0.2Z_\odot = 0.004$). In addition, to take into account the strong contribution from nebular emission, we also considered STARBURST99 (SB99) templates (Leitherer et al. 1999) for young galaxies (age $\leqslant 10^7$ yr) with constant SFHs.

We adopted the Calzetti (2001) reddening law in combination with the Leitherer et al. (2002) prescription below 912 Å to convolve the model templates and account for dust extinction. We used a color-excess grid of $0 \leqslant E(B-V) \leqslant 1.5$, with a step of 0.1. We refer the reader to Rinaldi et al. (2022, 2023) for further details on the SED fitting procedure.

4. Selection of Strong (Hβ + [O III]) Emitters

From our galaxy catalog in the P2/NIRCam region, we considered all the galaxies with best-fit $5.5 < z_{\rm phot} < 7$, as given in the output file from LePHARE. To select which of these sources are prominent (Hβ + [O III]) emitters, we followed the same technique described in Rinaldi et al. (2023). Briefly, we analyzed which of the $5.5 < z_{\rm phot} < 7$ galaxies show a flux density excess (with respect to the continuum) in the NIRCam F356W band. To obtain the corresponding (Hβ + [O III]) line complex rest-frame equivalent width (EW$_0$), we measured the difference between the observed F356W flux density and the flux density of the best-fit continuum model in the same band. The latter has been obtained by repeating the SED fitting with the fixed, previously obtained redshift and excluding the F356W filter (to prevent any bias produced by the line emission).

We then adopted the formula provided by Mármol-Queraltó et al. (2016) to convert the flux excess into the line complex

---

[17] The official JWST pipeline is available at https://github.com/spacetelescope/jwst.

[18] For more information see JWST's documentation webpage.

[19] The HLF catalog is available at https://doi.org/10.17909/T91019.

[20] The HST images ($0.\!''03$ pixel^{-1}) have been downloaded from the Space Telescope Science Institute's archive.

EW_0, which for our case is:

$$EW_0 = W_{F356W} (10^{(-0.4\Delta mag)} - 1)/(1 + z), \quad (1)$$

where W_{F356W} is the rectangular width of the F356W filter and Δmag is the difference between the observed magnitude and the synthetic continuum magnitude in the F356W filter. To guarantee that the flux density excess in the F356W band was meaningful, we imposed that $\Delta mag < -0.1$, implying that we are sensitive to selecting galaxies with a minimum $EW_0 \approx 100$ Å (more precisely, $EW_0 \approx 107$ Å at $z = 5.5$ and $EW_0 \approx 87$ Å at $z = 7$). We obtained the error bars of each source's EW_0 by doing 1000 random realizations of the F356W photometry, assuming a Gaussian distribution whose rms is given by the F356W photometric errors.

To ensure that the continuum was well described by the best-fit SED, we require that $\Delta mag(F277W) < 2 \times error\_mag$ (F2777W). We did not impose a similar criterion for F444W, which is the filter next to the red side of F356W, because F444W may be affected by Hα emission at $5.5 \lesssim z_{phot} \lesssim 7$ and because we do not have F444W coverage in some cases.

Following these criteria, we found that 34 galaxies are prominent (Hβ + [O III]) emitters, among a total of 102 galaxies at $5.5 < z_{phot} < 7$ in our P2/NIRCam galaxy sample. For all the emitters, we verified the flux density excess in F356W by visual inspection. These strong (Hβ + [O III]) emitters constitute $\simeq 33\%$ of all galaxies at $5.5 < z_{phot} < 7$. This percentage is very similar to that reported by Rinaldi et al. (2023) at $z = 7$–8. Our derived EW_0 values range between $\simeq 94$ and 1695 Å, with a median of 363^{+335}_{-227} Åi. This is broadly consistent with the results from Endsley et al. (2023b), but significantly lower than the median value found by Rinaldi et al. (2023), i.e., 943^{+737}_{-194} Åi at $z = 7$–8. This may be suggesting a redshift evolution in the median EW_0 values (although see the comments in Section 5.1). A few examples of best-fit SEDs for our (Hβ + [O III]) emitters are shown in Figure 2.

We investigated the impact of adopting different photometric excess thresholds in F356W to select the line emitters in our sample. For example, if we consider a much stricter Δmag (F356W) < -0.2 mag cut, only 26 galaxies are classified as prominent (Hβ + [O III]) emitters. Instead, if we change the limit to $\Delta mag(F356W) < -0.07$ mag, we will have 38 galaxies classified as strong emitters. In any case, all the analysis that we present below is based jointly on our own data points and data points from the literature, so reasonably changing the flux excess threshold (and, thus, the selected sample of strong emitters) has little impact on our results and does not change any of our conclusions.

5. Properties of the (Hβ + [O III]) Emitters at $5.5 < z < 8$

5.1. General Properties

First we investigate how the EW_0(Hβ + [O III]) values are related to some basic galaxy properties derived from the SED fitting.

Figure 3 shows the (Hβ + [O III]) EW_0 versus rest-frame UV absolute magnitude ($M_{UV} = M(1500$ Å$)$) for each galaxy. In this figure, as well as all subsequent figures, we complement our data points from the P2/NIRCam (Hβ + [OIII]) line emitter sample with (Hβ + [O III]) emitters at $z \sim 5$–8 from the recent literature (Endsley et al. 2021; Prieto-Lyon et al. 2023; Endsley et al. 2023a;
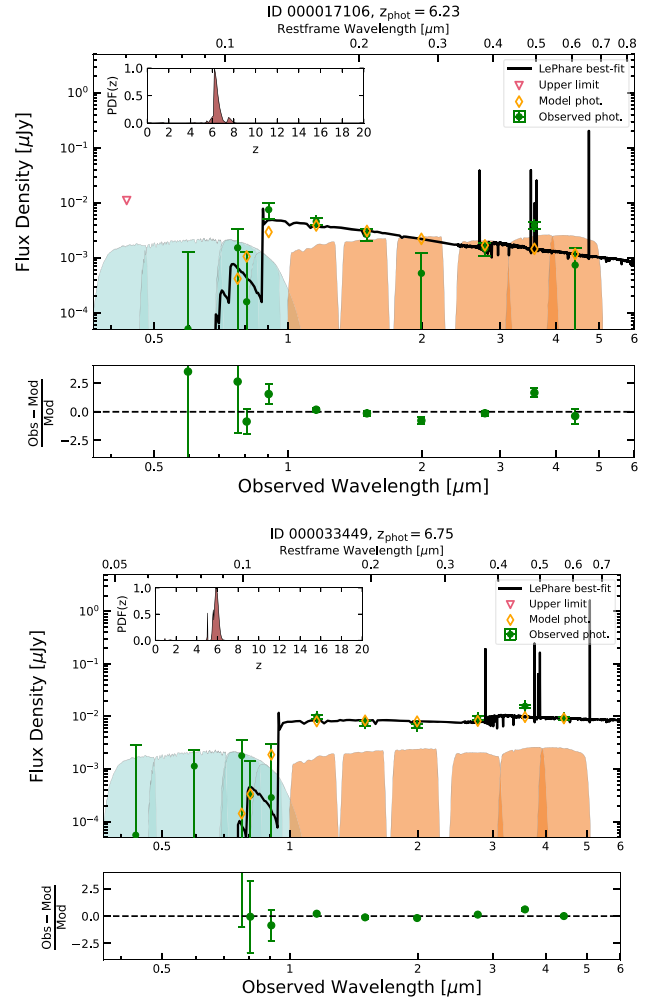

Figure 2. Examples of best-fit SEDs for two of our (Hβ + [O III]) emitters. The flux excess with respect to the continuum produced by the (Hβ + [O III]) line complex can be seen in the F356W filter. The green/orange shaded areas show the HST/JWST filter transmission curves. In both the top and bottom panels there is an inset showing the probability of the photometric redshift solution probability distribution function (PDF(z)).

Rinaldi et al. 2023; Endsley et al. 2023b). Most of these complementary samples also correspond to photometric selections of (Hβ + [O III]) emitters.

We observe no correlation between (Hβ + [O III]) EW_0 and M_{UV}, which indicates that the physical processes behind these two parameters are independent. Note that M_{UV} does not include any dust extinction correction, as it is typically the case for M_{UV} values in the literature. In any case, in our sample at $z = 5.5$–7 only four out of our 34 (Hβ + [O III]) line emitters have a best-fit color excess $E(B - V) > 0$.

With respect to the stellar mass, instead, both for our data points alone and for all data points considered together we observe a broad anticorrelation, such that lower-stellar-mass line emitters have on average higher values of EW_0(Hβ + [O III]) (see Figure 4). The existence of such an anticorrelation was already reported at different redshifts (e.g., Reddy et al. 2018; Endsley et al. 2021; Rinaldi et al. 2023).

Our galaxy sample reaches stellar masses about 1 dex lower ($\log_{10}(M^\star) = 6 - 7$) than any other from the samples shown in Figure 4, and lower than the minimum stellar masses probed at those redshifts with other JWST galaxy surveys (e.g., Navarro-Carrera et al. 2024). However, our galaxy sample is still
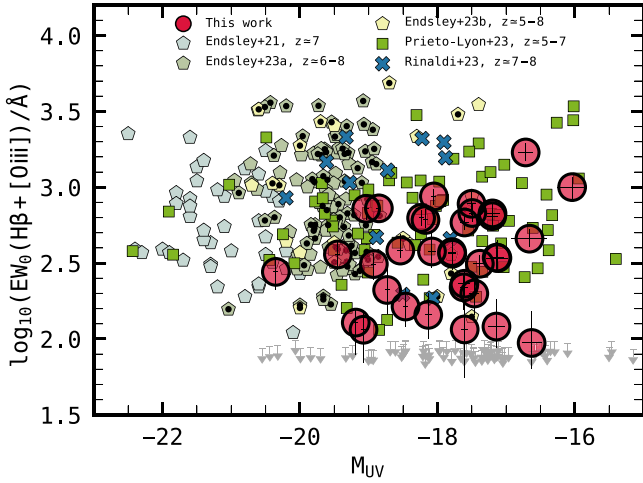
Figure 3. $EW_0(H\beta + [O\,III])$ vs. rest-frame UV absolute magnitude. No correlation is seen between these two parameters when all data points from this work and the literature are considered together. The literature data points with a black dot within correspond to galaxies at $z < 7$, where the dot has been added to differentiate the lower- and higher-redshift galaxies from the same literature sample. The gray downward-pointing arrows indicate upper limits corresponding to all the galaxies in our sample at $z = 5.5–7$ which are not classified as $(H\beta + [O\,III])$ emitters (referred to as "nonemitters" here).
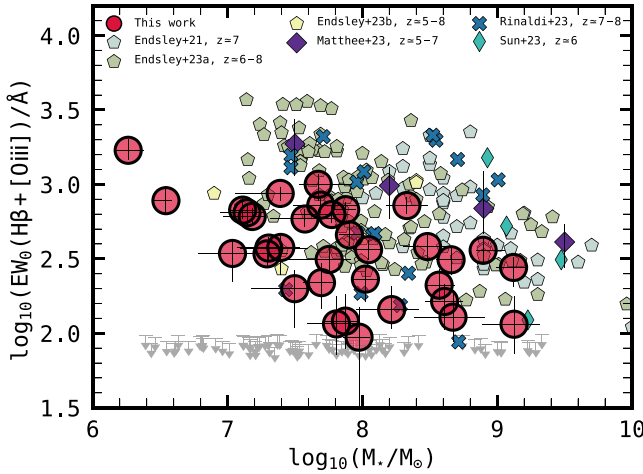
Figure 4. $EW_0(H\beta + [O\,III])$ vs. stellar mass. A broad anticorrelation between these two parameters is observed, in agreement with previous works.

incomplete at $\log_{10}(M^\star) < 7$. At these lowest stellar masses, we find only two prominent $(H\beta + [O\,III])$ emitters, both with $EW_0(H\beta + [O\,III]) \gtrsim 500$ Å, but we cannot discard the existence of other more modest line emitters with similarly low stellar masses. In addition to these two emitters with $\log_{10}(M^\star) = 6 - 7$, our galaxy sample at $z = 5.5–7$ in P2/NIRCam contains 13 galaxies in the same stellar-mass range which show no significant $(H\beta + [O\,III])$ flux density excess in the F356W filter (i.e., $EW_0(H\beta + [O\,III]) \lesssim 100$ Å; upper limits in Figure 4).

An important effect observed in Figure 4 is the lack of galaxies with stellar mass $\log_{10}(M^\star) > 9$ and $EW_0(H\beta + [O\,III]) \gtrsim 700$ Å (Figure 4). All the data sets considered here are deep enough to be basically complete at such stellar masses. Galaxies with $\log_{10}(M^\star) > 9$ and emission lines with $EW_0 \gtrsim 700$ Å do exist at high redshifts (e.g., Smit et al. 2016; Caputi et al. 2017), but are rare and can typically be found only in large-area surveys. In the small-area surveys that we consider here, line emitters with such high $EW_0(H\beta + [O\,III])$ are only found
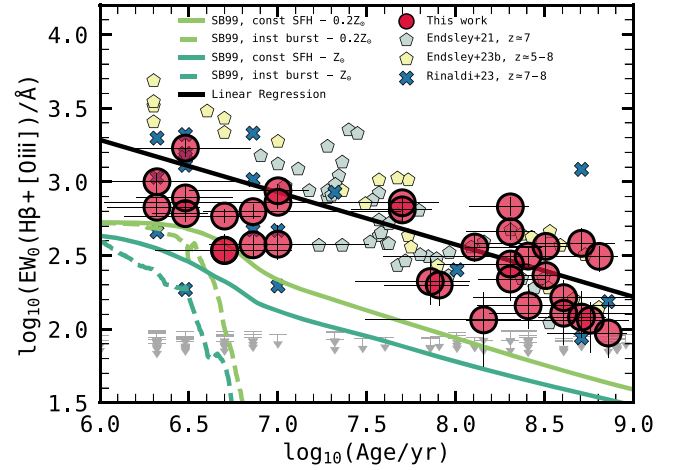
Figure 5. $EW_0(H\beta + [O\,III])$ vs. galaxy age. We also see an anticorrelation between these two parameters, which is related to the anticorrelation observed with respect to stellar mass (see Figure 4). The solid black line corresponds to the best-fit linear regression performed on our data points along with the data from the literature. The model tracks from SB99 shown with green lines correspond only to the $H\beta$ EW_0 and, thus, lie all below the observed data points.

among galaxies of stellar masses $M^\star < 10^9$ $M_\odot$. We argue below that the observed trend between $EW_0(H\beta + [O\,III])$ and stellar mass is mainly produced by the dependence of $EW_0(H\beta + [O\,III])$ with galaxy age.

Figure 5 shows the $EW_0(H\beta + [O\,III])$ versus the galaxy best-fit age. In this plot we see a similar effect to that in Figure 4: there is a broad anticorrelation which is valid for the identified strong line emitters. We performed a linear regression taking into account all data points and their errors. We obtained a slope $\alpha = -0.36^{+0.02}_{-0.01}$. About 35% of the emitters have very young ages ($\lesssim$30 Myr), while the remaining 65% correspond to older galaxies.

The youngest galaxies (with ages $\lesssim 30$ Myr) display a relatively wide range of $EW_0(H\beta + [O\,III])$ values ($EW_0(H\beta + [O\,III]) \gtrsim 300$ Å). Such a result can be explained with synthetic galaxy models and is related to the galaxy SFH, as can be seen in the stellar tracks in Figure 5: a galaxy passing through an instantaneous star formation burst will suffer a quick decline of the emission line EW_0 in only $\sim$10 Myr. Being young is a necessary (albeit not sufficient) condition for a galaxy to be among the strongest line emitters.

At the same time, virtually no galaxy with age $\gtrsim 30$ Myr has $EW_0 \gtrsim 700$ Å, even if they are still relatively strong emitters with $EW_0(H\beta + [O\,III])$ of up to several hundred angstroms. At these older ages, the line emission likely indicates more extended SFHs or possibly an early rejuvenation effect, as those that are more common at lower redshifts (e.g., Rosani et al. 2020; Iani et al. 2023).

Finally, we note that there is a large percentage ($\simeq$67%) of galaxies in our sample at $z = 5.5–7$ which do not show any F356W flux density excess, i.e., they have $(H\beta + [O\,III]) \lesssim 100$ Å, and span all ages between 10^6 and 10^9 yr.

5.2. Dependence on Star Formation Rate

In this section we investigate how the galaxy $EW_0(H\beta + [O\,III])$ is related to its SFR and position on the SFR–$M^\star$ plane.

Figure 6 shows the relation between $EW_0(H\beta + [O\,III])$ and SFR for our galaxies as well as other sources from the literature. The SFR has been derived from the rest-frame

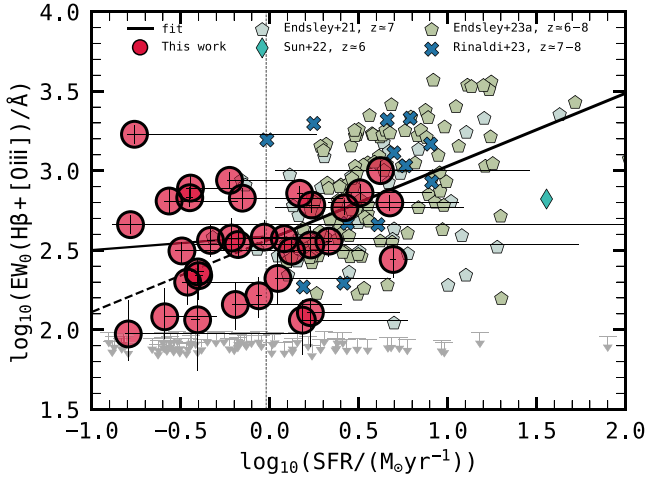**Figure 6.** $EW_0(H\beta + [O\,III])$ vs. galaxy SFR. Symbols are the same as in previous figures. The solid lines show the result of a two-component linear regression, which indicates a break in the EW_0–SFR relation at $\log_{10}(SFR/M_\odot\,yr^{-1}) = -0.02^{+0.08}_{-0.05}$. The dashed line indicates the extrapolation of the higher-SFR component, which helps to show how the relation flattens out at low-SFR values. The correlation break is produced by the high dispersion observed in the low-SFR regime, with some very high $EW_0(H\beta + [O\,III])$ values. This is likely the consequence of the dominant effect of [O III], and thus very low metallicities, in some galaxies with lower SFRs.

UV ($\lambda_{rest} = 1500$ Å) galaxy luminosity in each case, so it is independent of the $EW_0(H\beta + [O\,III])$ measurement. In turn, this UV luminosity has been obtained from the observed photometry in the filter that most closely encompasses the galaxy rest-frame 1500 Å light at the source redshift. Thanks to the depth of the NIRCam imaging in P2/NIRCam, we can probe galaxies down to unprecedented low-SFR values, i.e., $SFR \approx 0.1\ M_\odot\ yr^{-1}$, at $z = 5.5$–7.

In contrast to the quite monotonic trend observed with respect to other galaxy parameters (age and stellar mass), the relation between $EW_0(H\beta + [O\,III])$ and SFR shows a more complex behavior. Considering our data points jointly with those from the literature, we see that $EW_0(H\beta + [O\,III])$ and SFR broadly correlate with each other at $SFR \gtrsim 1\ M_\odot\ yr^{-1}$, but this correlation flattens out at smaller SFR values. We performed a two-component Bayesian linear regression taking into account all data points and their errors, using the python tool pyro.[21] We obtained that the break point of the EW_0–SFR relation occurs at $\log_{10}(SFR/M_\odot\,yr^{-1}) = -0.02^{+0.08}_{-0.05}$. The slope of the relation changes from 0.46 ± 0.02 at higher SFRs to $0.09^{+0.09}_{-0.08}$ at lower SFRs. Indeed, at $SFR \lesssim 1\ M_\odot\ yr^{-1}$, galaxies display a wide range of possible $EW_0(H\beta + [O\,III])$ values and no correlation is observed any more with the galaxy SFR.

In principle, one would expect that the behavior of $EW_0(H\beta + [O\,III])$ versus SFR is similar to that of $EW_0(H\beta + [O\,III])$ versus M_{UV}. However, the M_{UV} values in Figure 3 are not corrected for dust extinction (as is usual in the literature), while the SFR values are. This only affects four (out of 34) emitters in our sample, but also brighter galaxies from the other considered data sets. The four emitters whose SFR are dust corrected end up having $SFR > 1\ M_\odot\ yr^{-1}$, so they make part of the positive correlation observed at these higher-SFR values, but they are not responsible for it.

The positive correlation between $EW_0(H\beta + [O\,III])$ and SFR obtained at $SFR > 1\ M_\odot\ yr^{-1}$ is mainly driven by the data points from the literature. Note also that, for some of them, the SFR values have been calculated from best-fit SED models, in contrast to our own values and those of, e.g., Rinaldi et al. (2023), which have been empirically obtained directly from the galaxy rest-frame UV luminosities and are independent of the SED fitting. In any case, a comparison of these methodologies to compute the SFR (based on our own data) indicates that there should not be any systematic effect and, therefore, the resulting break observed in the correlation at $SFR \simeq 1\ M_\odot\ yr^{-1}$ in Figure 6 should be robust against these methodology differences.

We tested the sensitivity of the EW_0–SFR correlation break to our adopted threshold of flux density excess to select strong line emitters. As explained above, if we lowered the threshold to $\Delta mag(F356W) < -0.07$ mag, then there would be 38 strong $(H\beta + [O\,III])$ emitters in our sample (instead of 34). We repeated the two-component linear regression considering all these galaxies along with the literature data points. We found that the break is similarly significant as that show in Figure 6 and the break point shifts only slightly to $\log_{10}(SFR/M_\odot\,yr^{-1}) \approx -0.05$. We also checked that the break is not driven by the inclusion of literature data points up to $z = 8$, i.e., beyond the redshift limits of our own sample. If we repeat the analysis considering only literature data points up to $z = 7$, we still find a significant correlation break with a break point at $\log_{10}(SFR/M_\odot\,yr^{-1}) \approx -0.08$.

This change of trend in the $(H\beta + [O\,III])$ line complex behavior suggests that the $(H\beta + [O\,III])$ line complex might be dominated by different physical processes at low and high SFRs. The positive correlation at $SFR \gtrsim 1\ M_\odot\ yr^{-1}$ indicates that the strength of [O III] must be following the SFR, as $H\beta$ more obviously does. At lower SFR, instead, $H\beta$ must become less important and, thus, the $EW_0(H\beta + [O\,III])$ value might be virtually dominated by [O III]. The high dispersion observed in this low-SFR regime, with some very high $EW_0(H\beta + [O\,III])$ values, suggests that decreasing gas metallicities may be the main reason for the increasing $EW_0(H\beta + [O\,III])$ with decreasing SFR. Low metallicities are linked to higher radiation fields (e.g., Kumari et al. 2021), which in turn produce more prominent nebular lines, i.e., nebular lines with higher EWs.

A roughly similar effect is observed from spectroscopic studies at lower redshifts, particularly Figure 6 in Reddy et al. (2018), although in this work the SFR regimes below and above $SFR \approx 1\ M_\odot\ yr^{-1}$ are probed at different redshifts ($z = 0$ and $z \sim 1.5$–3.8, respectively). The separate analyses of the $H\beta$ and [O III] EWs in that work indicate that, as expected, it is the [O III] emission line that drives the trend break at low SFR.

As it was the case for low-stellar-mass galaxies, many of the galaxies with $SFR < 1\ M_\odot\ yr^{-1}$ in our sample are actually not prominent line emitters, i.e., have $EW_0(H\beta + [O\,III]) \lesssim 100$ Å (shown as upper limits in Figure 6). So once again the discussed trends only apply to the subset of galaxies that do show line emission. As we discuss throughout this paper, if star formation activity proceeds in bursts rather than continuously, then emission lines are only expected to be present at very young ages ($\lesssim 10$ Myr). Instead, the rest-frame UV continuum emission indicative of ongoing star formation lasts longer.

As a matter of fact, at young galaxy ages, deriving the SFR from rest-frame UV fluxes in the canonical manner is not strictly correct. Most SFR tracers stabilize only after ~ 100 Myr
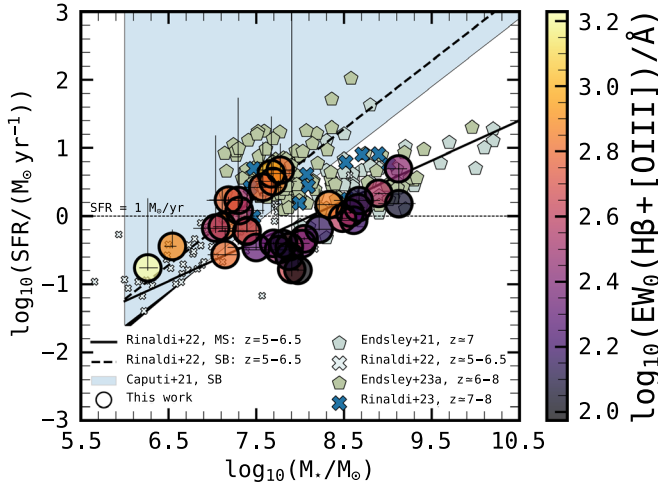
Figure 7. Location of our galaxies in the SFR–$M^\star$ plane, color coded according to their $EW_0(H\beta + [O\,III])$ values. As in previous figures, we complement our galaxy sample with other samples from the literature at $z = 5$–8 (Endsley et al. 2021; Rinaldi et al. 2022; Endsley et al. 2023a; Prieto-Lyon et al. 2023; Rinaldi et al. 2023). The light-blue shaded region indicates the starburst zone, as defined in Caputi et al. (2017, 2021).

Figure 8. $EW_0(H\beta + [O\,III])$ vs. galaxy sSFR. Symbols are the same as in previous figures. The light-blue shaded region indicates the starburst zone, as defined in Caputi et al. (2017, 2021).

(Otí-Floranes & Mas-Hesse 2010) and indeed the Kennicutt (1998) prescription assumes a constant SFH for 100 Myr. The youngest galaxies in our sample, including most of the line emitters, do not comply with this assumption. We tested the impact of deriving SFR values based on rest-frame UV luminosities with the Kennicutt (1998) empirical law for these very young sources, in order to understand whether their presence has any influence in our conclusions. For this, we corrected the derived SFR by the expected SFR(Hα)/SFR(UV) ratios at different ages, following the tracks shown in Figure 15 of Iani et al. (2023), which are in turn based on BPASS synthetic galaxy models (Eldridge et al. 2017; Stanway & Eldridge 2018). We found that applying these corrections does not have any significant impact in our results and conclusions.

5.3. The SFR–$M^\star$ Plane

Figure 7 shows the location of our (Hβ + [O III]) emitters at $z = 5.5$–7, along with other galaxies at $z = 5$–8 from the literature, on the SFR–$M^\star$ plane. Our (Hβ + [O III]) emitters are color coded according to their $EW_0(H\beta + [O\,III])$ values.

The (Hβ + [O III]) emitters occupy different regions of the SFR–$M^\star$ plane, with some being located in the star formation MS (e.g., Speagle et al. 2014) and others in the starburst zone, empirically defined as the half-plane with $\log_{10}(sSFR(yr^{-1})) > -7.6$ (Caputi et al. 2017, 2021). According to this definition, starbursts are galaxies with a stellar-mass doubling time $\lesssim 40$ Myr, consistently with local starbursts (Kennicutt 1998). From Figure 7, it is evident that the strongest line emitters are preferentially found among the starburst galaxies. These (Hβ + [O III]) emitters in the starburst zone span a wide range of stellar masses, between $\log_{10}(M^\star/M_\odot) \approx 6$ and ≈ 9.

We see that the star formation MS and starburst cloud converge on the SFR–$M^\star$ plane at SFR $\approx 0.3\ M_\odot$ yr^{-1}, i.e., a somewhat lower value than the break SFR discussed in Section 5.2. This intersection was predicted by Rinaldi et al. (2022) from the extrapolation of the two star-forming mode trends towards low stellar masses at high redshifts. The depth of our new JWST data in P2/NIRCam allows us to directly detect a few galaxies there. In this regime of low stellar masses
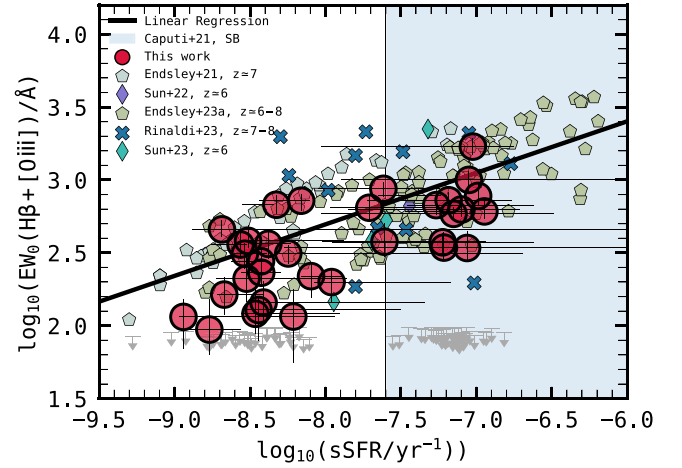
and SFRs, all star formation should be proceeding in a single mode and the gap between the star formation MS and starbursts disappears.

Finally, we show the relation between $EW_0(H\beta + [O\,III])$ and sSFR in Figure 8. Here we also observe a positive correlation, such that the most prominent (Hβ + [O III]) emitters tend to have higher sSFR values. In this case, for the best-fit linear regression we obtain a slope $\alpha = 0.35 \pm 0.01$. Particularly, the most extreme emitters are mostly found in the starburst zone. For example, if we consider all those galaxies with $EW_0 > 700$ Å, we find that $\simeq 70\%$ of them are starbursts. Instead, among the line emitters with lower $EW_0(H\beta + [O\,III])$, only $\simeq 25\%$ are in the starburst region.

A cross-correlation between $EW_0(H\beta + [O\,III])$ and sSFR, even if broad, is not trivial. We do expect a galaxy sSFR to be more directly related to the $EW_0(H\alpha)$, as the Hα luminosity provides a fiducial measurement of the galaxy SFR, while the continuum at the Hα rest-frame wavelength is roughly proportional to the galaxy stellar mass. Instead, the (Hβ + [O III]) line complex is expected to be dominated by the [O III] emission in most cases (e.g., Cameron et al. 2023; Langeroodi et al. 2023), making the total (Hβ + [O III]) luminosity to depend not only on the galaxy SFR, but also, e.g., its gas temperature and metallicity. All these properties will affect the $EW_0(H\beta + [O\,III])$ values.

In any case, it is important to note that the observed trend between $EW_0(H\beta + [O\,III])$ and sSFR also applies exclusively to galaxies with identified (Hβ + [O III]) emission. In our own sample in P2/NIRCam, we have 68 galaxies at $z = 5.5$–7 with no (Hβ + [O III]) flux density excess in the F356W filter. And, among these nonemitters, $\simeq 55\%$ are starburst galaxies, although this percentage should be considered an upper limit because a flux-limited galaxy survey will mainly prevent the selection of galaxies with low sSFR at fixed stellar mass (P. Rinaldi et al. 2024, in preparation). In summary, the starburst region does not contain only galaxies with high $EW_0(H\beta + [O\,III])$ values, but those which do have such high EW_0 values are preferentially found in a starbursting phase.

As discussed before, the fact that there are many galaxies which are starbursts, but have low values of $EW_0(H\beta + [O\,III])$ is likely related to the fact that the rest-frame UV galaxy luminosity and the Balmer lines do not trace star formation

activity over the same timescales (e.g., Sparre et al. 2017; Faisst et al. 2019). The rest-frame UV luminosity is produced by O- and B-type stars, so it typically indicates star formation activity on timescales of $\sim$100 Myr. Instead, in galaxies passing through a burst of star formation, Balmer lines will sharply decrease their luminosities after a few tens of megayears (e.g., Iglesias-Páramo et al. 2004; Lee et al. 2009; Otí-Floranes & Mas-Hesse 2010; Guo et al. 2016; Emami et al. 2019; Iani et al. 2023).

6. Summary and Discussion

In this paper we investigated the dependence of strong (Hβ + [O III]) emission (EW$_0$(Hβ + [O III]) $\gtrsim$ 100 Å) on the main host galaxy properties, particularly those that are derived from SED fitting, at $z = 5.5$–8. Considering jointly our own data and recent results from the literature has been important to increase the statistics of our analysis, as well as (at least partly) homogenizing the possible selection effects from the different data sets. Moreover, by studying also the nonemitters in our sample at comparable redshifts, we could also put the emitters in the more general context of galaxy evolution around the Epoch of Reionization.

For the strong (Hβ + [O III]) emitters we found broad anticorrelations between the EW$_0$(Hβ + [O III]) and both galaxy stellar mass and age. These two EW$_0$(Hβ + [O III]) anticorrelations are not independent: the most massive galaxies ($\log_{10}(M^\star/M_\odot) > 8$) are among the oldest ones ($\log_{10}(\text{age}) \gtrsim 7.5$) at $z = 5$–8. However, the roles of these two parameters are different. While a higher stellar mass would mainly decrease the EW$_0$(Hβ + [O III]) by increasing the underlying continuum light, galaxy age would directly affect the emission line luminosities, as it is expected from galaxy spectral models (Leitherer et al. 1999). Similar trends have previously been reported in the literature at different redshifts (e.g., Khostovan et al. 2016; Reddy et al. 2018; Endsley et al. 2021; Boyett et al. 2022; Matthee et al. 2023), which suggest that the physics driving strong line emitters is basically the same through cosmic time.

We observe only a very tentative evolution of these trends in the redshift range analyzed here $z = 5.5$–8. This is perhaps not surprising given the corresponding short elapsed time ($\sim$0.5 Gyr), but still interesting to remark given that this period comprises the epoch before and after the end of reionization.

A key result of this paper is the finding that the relation between EW$_0$(Hβ + [O III]) and the galaxy SFR could change at SFR $\lesssim 1 \, M_\odot \, \text{yr}^{-1}$. The unprecedented depth of our NIRCam data allows us to explore such low-SFR values for nonlensed galaxies at $z = 5.5$–7. Indeed, the correlation observed between EW$_0$(Hβ + [O III]) and SFR at SFR $\gtrsim 1 \, M_\odot \, \text{yr}^{-1}$ flattens out at SFR $\lesssim 1 \, M_\odot \, \text{yr}^{-1}$, which suggests that in this regime the (Hβ + [O III]) complex is dominated by the [O III] line and galaxies may have lower metallicities towards lower SFR values. Indeed, this has been shown to be the case at low redshifts (Duarte Puertas et al. 2022). Low metallicities are linked to high radiation fields, which in turn are responsible for higher luminosities (and EWs) in nebular lines. Unfortunately the current data do not allow us to directly constrain the galaxy metallicities, except crudely via the SED modeling. As expected, the majority ($\gtrsim$70%) of our galaxies have a best-fit SED with subsolar metallicity, including those with the lowest-stellar-mass and SFR values.

We note that incompleteness may be affecting our sample at SFR $\lesssim 1 \, M_\odot \, \text{yr}^{-1}$, i.e., there may be undetected galaxies which

have such low SFRs and significant (Hβ + [O III]) emission (with EW$_0$(Hβ + [O III]) $\gtrsim$ 100 Å). These possibly missing galaxies could lie close to the extrapolation of the EW$_0$(Hβ + [O III])–SFR correlation for SFR $\gtrsim 1 \, M_\odot \, \text{yr}^{-1}$ at SFR $\lesssim 1 \, M_\odot \, \text{yr}^{-1}$, but still the sources with low SFR and high EW$_0$(Hβ + [O III]) will be present, indicating that a simple correlation cannot explain the behavior of all sources at low SFR.

Another possibility to explain the break in the EW$_0$(Hβ + [O III]) versus SFR relation at SFR $\approx 1 \, M_\odot \, \text{yr}^{-1}$ is that at low SFR the spectral line emission can be affected by stochastic sampling of the galaxy star formation and/or IMF (e.g., Boissier et al. 2007; Lee et al. 2009; da Silva et al. 2012; Forero-Romero & Dijkstra 2013; Mas-Ribas et al. 2016). These kinds of effects only matter at very low SFR ($\sim$0.1 $M_\odot \, \text{yr}^{-1}$) at low redshifts, but the bursty nature characterizing many high-z galaxies may still produce a stochastic sampling of the star-forming units within a galaxy (Vikaeus et al. 2020; Pallottini & Ferrara 2023). This, in turn, can have important implications for the estimation of metallicities in low-SFR galaxies at high redshifts (e.g., Vanzella et al. 2023).

In any case, we note that our results suggesting low metallicities for starbursting low-stellar-mass galaxies are in line with the predictions of galaxy formation models. Using the ASTRAEUS galaxy formation framework (Hutter et al. 2021), which couples galaxy formation with reionization, Ucci et al. (2023) showed that the mass–metallicity relation of galaxies around the Epoch of Reionization depends on their sSFR, such that higher sSFR values correspond to lower metallicities at fixed stellar mass. This is explained because galaxies with a higher sSFR had stronger outflows and, thus, a higher amount of metal ejection, leaving their interstellar medium less metal enriched.

The location of the (Hβ + [O III]) emitters on the SFR–$M^\star$ plane shows also a break in the star formation MS–starburst bimodality towards low-SFR values, albeit at somewhat lower SFR than the SFR turning point in the EW$_0$(Hβ + [O III])–SFR relation. The convergence of the two sequences was discussed by Rinaldi et al. (2022) and suggests that all star formation happens in a single mode at the lowest-stellar-mass galaxies. Our current ultradeep observations allow us to directly see a few galaxies in this convergence regime.

In general, the highest EW$_0$(Hβ + [O III]) values are also associated with high sSFR and, correspondingly, with a high incidence of the strongest (Hβ + [O III]) emitters in the starburst region of the SFR–$M^\star$ plane ($\sim$70% of those with EW$_0$(Hβ + [O III]) > 700 Å are starbursts). This result agrees with the findings of Boyett et al. (2022) and Endsley et al. (2023a), who suggested that the brightest line emitters at high redshifts could be experiencing a strong upturn in their SFR. It is also in line with the results derived from the FirstLight galaxy simulation (Ceverino et al. 2017, 2018), which predict a correlation between EW$_0$[O III] and galaxy sSFR, although only a very small fraction of their simulated galaxies have the high sSFR values characterizing our starburst galaxies at $z = 5.5$–7 (Ceverino et al. 2021).

Considering the galaxy properties analyzed here altogether allow us to conclude that the strongest line emitters are typically young, low-stellar-mass galaxies that are starbursting or very close to the starburst phase. These makes them favorite candidates for the sources of reionization, as their ionizing photon production efficiency could be significantly higher than

for other galaxies (Izotov et al. 2018; Rinaldi et al. 2024; Simmonds et al. 2024).

Throughout this work we have analyzed the properties of the strong (Hβ + [O III]) emitters at $z = 5.5$–7 in comparison to those of all other sources (which we called nonemitters) at similar redshifts. The strong emitters constitute only ~33% of all the galaxies at $z = 5.5$–7 in our P2/NIRCam sample, in broad agreement with the percentage reported in the literature for $z = 7$–8 (Rinaldi et al. 2023). We found that many nonemitters share the same properties as the typical strong emitters, i.e., low stellar masses, young ages, and high sSFR. This strongly suggests that the strong line emitters are not different in nature to many other galaxies at $z = 5.5$–7.0; they are rather the same kinds of galaxies just passing through the initial stages of a burst of star formation. At their flux limit, galaxy surveys will preferentially contain strong line emitters, as the emission line can boost their observability (e.g., Sun et al. 2023).

These results considered together suggest that all young, low-stellar-mass, star-forming galaxies at such high redshifts could have had a role in reionization. Their importance as ionizing sources was maximum at the beginning of the starburst phase. Ultradeep spectroscopic studies to be conducted with JWST are necessary to better understand the physical conditions associated with star formation in young, low-stellar-mass galaxies.

Acknowledgments

ORCID iDs

K. I. Caputi ⓘ https://orcid.org/0000-0001-8183-1460
P. Rinaldi ⓘ https://orcid.org/0000-0002-5104-8245
E. Iani ⓘ https://orcid.org/0000-0001-8386-3546
P. G. Pérez-González ⓘ https://orcid.org/0000-0003-4528-5639
G. Östlin ⓘ https://orcid.org/0000-0002-3005-1349
L. Colina ⓘ https://orcid.org/0000-0002-9090-4227
T. R. Greve ⓘ https://orcid.org/0000-0002-2554-1837
H. U. Nørgaard-Nielsen ⓘ https://orcid.org/0000-0000-0000-0000
G. S. Wright ⓘ https://orcid.org/0000-0000-0000-0000
J. Álvarez-Márquez ⓘ https://orcid.org/0000-0002-7093-1877
A. Eckart ⓘ https://orcid.org/0000-0001-6049-3132
J. Hjorth ⓘ https://orcid.org/0000-0002-4571-2306
A. Labiano ⓘ https://orcid.org/0000-0002-0690-8824
O. Le Fèvre ⓘ https://orcid.org/0000-0001-5891-2596
F. Walter ⓘ https://orcid.org/0000-0003-4793-7880
P. van der Werf ⓘ https://orcid.org/00000-0001-5434-5942
L. Boogaard ⓘ https://orcid.org/0000-0002-3952-8588

L. Costantin ⓘ https://orcid.org/0000-0001-6820-0015
A. Crespo Gómez ⓘ https://orcid.org/0000-0003-2119-277X
S. Gillman ⓘ https://orcid.org/0000-0001-9885-4589
I. Jermann ⓘ https://orcid.org/0000-0002-2624-1641
D. Langeroodi ⓘ https://orcid.org/0000-0001-5710-8395
J. Melinder ⓘ https://orcid.org/0000-0003-0470-8754
F. Peissker ⓘ https://orcid.org/0000-0000-0000-0000
M. Güdel ⓘ https://orcid.org/0000-0001-9818-0588
Th. Henning ⓘ https://orcid.org/0000-0002-1493-300X
P. O. Lagage ⓘ https://orcid.org/0000-0000-0000-0000
T. P. Ray ⓘ https://orcid.org/0000-0002-2110-1068

References

Arnouts, S., & Ilbert, O., 2011 LePHARE: Photometric Analysis for Redshift Estimate, ASCL.netAstrophysics Source Code Library, ascl:1108.009
Austin, D., Adams, N. J., Conselice, C. J., et al. 2023, ApJL, 952, L7
Bertin, E., & Arnouts, S. 1996, A&AS, 117, 393
Bisigello, L., Caputi, K. I., Grogin, N., & Koekemoer, A. 2018, A&A, 609, A82
Boissier, S., Gil de Paz, A., Boselli, A., et al. 2007, ApJS, 173, 524
Boyett, K., Mascia, S., Pentericci, L., et al. 2022, ApJL, 940, L52
Brinchmann, J., Charlot, S., White, S. D. M., et al. 2004, MNRAS, 351, 1151
Bruzual, G., & Charlot, S. 2003, MNRAS, 344, 1000
Bushouse, H., Eisenhamer, J., Dencheva, N., et al. 2022, JWST Calibration Pipeline, Zenodo, 10.5281/ZENODO.7314521
Calzetti, D. 2001, NewAR, 45, 601
Cameron, A. J., Saxena, A., Bunker, A. J., et al. 2023, A&A, 677, A115
Caputi, K. I., Caminha, G. B., Fujimoto, S., et al. 2021, ApJ, 908, 146
Caputi, K. I., Deshmukh, S., Ashby, M. L. N., et al. 2017, ApJ, 849, 45
Ceverino, D., Glover, S. C. O., & Klessen, R. S. 2017, MNRAS, 470, 2791
Ceverino, D., Hirschmann, M., Klessen, R. S., et al. 2021, MNRAS, 504, 4472
Ceverino, D., Klessen, R. S., & Glover, S. C. O. 2018, MNRAS, 480, 4842
Chabrier, G. 2003, PASP, 115, 763
da Silva, R. L., Fumagalli, M., & Krumholz, M. 2012, ApJ, 745, 145
De Barros, S., Oesch, P. A., Labbé, I., et al. 2019, MNRAS, 489, 2355
Dressler, A., Rieke, M., Eisenstein, D., et al. 2024, ApJ, 964, 150
Duarte Puertas, S., Vilchez, J. M., Iglesias-Páramo, J., et al. 2022, A&A, 666, A186
Eldridge, J. J., Stanway, E. R., Xiao, L., et al. 2017, PASA, 34, e058
Emami, N., Siana, B., Weisz, D. R., et al. 2019, ApJ, 881, 71
Endsley, R., Stark, D. P., Chevallard, J., & Charlot, S. 2021, MNRAS, 500, 5229
Endsley, R., Stark, D. P., Whitler, L., et al. 2023a, MNRAS, 524, 2312
Endsley, R., Stark, D. P., Whitler, L., et al. 2023b, arXiv:2306.05295
Faisst, A. L., Capak, P. L., Emami, N., Tacchella, S., & Larson, K. L. 2019, ApJ, 884, 133
Forero-Romero, J. E., & Dijkstra, M. 2013, MNRAS, 428, 2163
Guo, Y., Rafelski, M., Faber, S. M., et al. 2016, ApJ, 833, 37
Heckman, T. M., Robert, C., Leitherer, C., Garnett, D. R., & van der Rydt, F. 1998, ApJ, 503, 646
Hutter, A., Dayal, P., Yepes, G., et al. 2021, MNRAS, 503, 3698
Iani, E., Caputi, K. I., Rinaldi, P., et al. 2023, ApJ, 963, 97

Iglesias-Páramo, J., Boselli, A., Gavazzi, G., & Zaccardo, A. 2004, A&A, 421, 887
Illingworth, G. 2015, Hubble Legacy Fields ("HLF"), STScI/MAST,
Izotov, Y. I., Worseck, G., Schaerer, D., et al. 2018, MNRAS, 478, 4851
Kennicutt, R. C. J. 1998, ARA&A, 36, 189
Khostovan, A. A., Sobral, D., Mobasher, B., et al. 2016, MNRAS, 463, 2363
Kron, R. G. 1980, ApJS, 43, 305
Kumari, N., Amorín, R., Pérez-Montero, E., Vílchez, J., & Maiolino, R. 2021, MNRAS, 508, 1084
Langeroodi, D., Hjorth, J., Chen, W., et al. 2023, ApJ, 957, 39
Lee, J. C., Gil de Paz, A., Tremonti, C., et al. 2009, ApJ, 706, 599
Leitherer, C., Li, I. H., Calzetti, D., & Heckman, T. M. 2002, ApJS, 140, 303
Leitherer, C., Schaerer, D., Goldader, J. D., et al. 1999, ApJS, 123, 3
Mármol-Queraltó, E., McLure, R. J., Cullen, F., et al. 2016, MNRAS, 460, 3587
Mas-Ribas, L., Dijkstra, M., & Forero-Romero, J. E. 2016, ApJ, 833, 65
Matthee, J., Mackenzie, R., Simcoe, R. A., et al. 2023, ApJ, 950, 67
Navarro-Carrera, R., Rinaldi, P., Caputi, K. I., et al. 2024, ApJ, 961, 207
Oke, J. B., & Gunn, J. E. 1983, ApJ, 266, 713
Östlin, G., Zackrisson, E., Bergvall, N., & Rönnback, J. 2003, A&A, 408, 887
Otí-Floranes, H., & Mas-Hesse, J. M. 2010, A&A, 511, A61
Pallottini, A., & Ferrara, A. 2023, A&A, 677, L4
Peng, Y.-j., Lilly, S. J., Kovač, K., et al. 2010, ApJ, 721, 193
Pérez-González, P. G., Costantin, L., Langeroodi, D., et al. 2023, ApJL, 951, L1
Prieto-Lyon, G., Strait, V., Mason, C. A., et al. 2023, A&A, 672, A186
Reddy, N. A., Shapley, A. E., Sanders, R. L., et al. 2018, ApJ, 869, 92
Renzini, A., & Peng, Y.-j. 2015, ApJL, 801, L29
Rinaldi, P., Caputi, K. I., Costantin, L., et al. 2023, ApJ, 952, 143
Rinaldi, P., Caputi, K. I., Iani, E., et al. 2024, ApJ, 969, 12
Rinaldi, P., Caputi, K. I., van Mierlo, S. E., et al. 2022, ApJ, 930, 128
Roberts-Borsani, G. W., Bouwens, R. J., Oesch, P. A., et al. 2016, ApJ, 823, 143
Rosani, G., Caminha, G. B., Caputi, K. I., & Deshmukh, S. 2020, A&A, 633, A159
Salmon, B., Papovich, C., Finkelstein, S. L., et al. 2015, ApJ, 799, 183
Simmonds, C., Tacchella, S., Hainline, K., et al. 2024, MNRAS, 527, 6139
Smit, R., Bouwens, R. J., Labbé, I., et al. 2014, ApJ, 784, 58
Smit, R., Bouwens, R. J., Labbé, I., et al. 2016, ApJ, 833, 254
Sobral, D., Smail, I., Best, P. N., et al. 2013, MNRAS, 428, 1128
Sonnett, S., Meech, K., Jedicke, R., et al. 2013, PASP, 125, 456
Sparre, M., Hayward, C. C., Feldmann, R., et al. 2017, MNRAS, 466, 88
Speagle, J. S., Steinhardt, C. L., Capak, P. L., & Silverman, J. D. 2014, ApJS, 214, 15
Stanway, E. R., & Eldridge, J. J. 2018, MNRAS, 479, 75
Sun, G., Faucher-Giguére, C.-A., Hayward, C. C., & Shen, X. 2023, MNRAS, 526, 2665
Tody, D. 1986, Proc. SPIE, 627, 733
Tody, D. 1993, in ASP Conf. Ser. 52, Astronomical Data Analysis Software and Systems II, ed. R. J. Hanisch, R. J. V. Brissenden, & J. Barnes (San Francisco, CA: ASP), 173
Ucci, G., Dayal, P., Hutter, A., et al. 2023, MNRAS, 518, 3557
Vanzella, E., Loiacono, F., Bergamini, P., et al. 2023, A&A, 678, A173
Vikaeus, A., Zackrisson, E., & Binggeli, C. 2020, MNRAS, 492, 1706
Whitaker, K. E., Ashas, M., Illingworth, G., et al. 2019, ApJS, 244, 16
Williams, C. C., Tacchella, S., Maseda, M. V., et al. 2023, ApJS, 268, 64